



Multiscale numerical modeling of solid particle penetration and hydrocarbons removal in a catalytic stripper

Mino Woo, George Giannopoulos, Md Mostafizur Rahman, Jacob Swanson, Marc E. J. Stettler & Adam M. Boies

To cite this article: Mino Woo, George Giannopoulos, Md Mostafizur Rahman, Jacob Swanson, Marc E. J. Stettler & Adam M. Boies (2021) Multiscale numerical modeling of solid particle penetration and hydrocarbons removal in a catalytic stripper, *Aerosol Science and Technology*, 55:9, 987-1000, DOI: [10.1080/02786826.2021.1909700](https://doi.org/10.1080/02786826.2021.1909700)

To link to this article: <https://doi.org/10.1080/02786826.2021.1909700>



© 2021 The Author(s). Published with license by Taylor & Francis Group, LLC.



[View supplementary material](#)



Published online: 26 Apr 2021.



[Submit your article to this journal](#)



Article views: 584



[View related articles](#)



[View Crossmark data](#)



Citing articles: 2 [View citing articles](#)



Multiscale numerical modeling of solid particle penetration and hydrocarbons removal in a catalytic stripper

Mino Woo^{a,b,*} , George Giannopoulos^b, Md Mostafizur Rahman^c, Jacob Swanson^d , Marc E. J. Stettler^a , and Adam M. Boies^b

^aDepartment of Civil and Environmental Engineering, Imperial College London, London, United Kingdom; ^bDepartment of Engineering, University of Cambridge, Cambridge, United Kingdom; ^cInstitute for Future Transportation and Cities, School of Mechanical Aerospace and Automotive Engineering, Coventry University, Coventry, United Kingdom; ^dDepartment of Integrated Engineering, Minnesota State University, Mankato, Minnesota, USA

ABSTRACT

The catalytic stripper has emerged as a technology for removal of semivolatile material from aerosol streams for automotive and aerospace emissions measurements, including portable solid particle emissions measurements governed by the Real Driving Emissions regulations. This study employs coupled energy and mass transfer models to predict solid particle penetration and hydrocarbon removal for various configurations of a catalytic stripper. The continuum-scale macromodel applies mass, momentum and energy conservation for the inlet heating region of a catalytic stripper whereby the catalyst monolith is represented by a porous medium. The particle and species dynamics inside the catalytic monolith were computed by coupled microsimulations of the monolith channel using boundary conditions from the macromodel. The results from the numerical simulations were validated with corresponding experimental data and employed using a parametric study of flow rate and catalyst length with a view to optimizing the operating condition. Results of the simulation and experiment show that solid particle penetration through the catalytic stripper can exceed approximately 60% for particles at 10 nm mobility diameter and hydrocarbons removal of >95% for an optimized catalytic stripper device.

ARTICLE HISTORY

Received 14 January 2021
Accepted 22 March 2021

EDITOR

Matti Maricq

1. Introduction

Improved air quality and reduced emissions are urgent worldwide public health, technological and political priorities. Particle emissions composed of black carbon, primary organic aerosols and secondary organic compounds are harmful to human health (Künzi et al. 2015). Highly populated urban areas particularly suffer from high concentrations of these exhaust emissions, which has motivated tightening emissions regulations. In addition to diesel exhaust that is generally perceived as the major contributor to urban air pollution, modern vehicles employing gasoline direct injection (GDI) without a gasoline particulate filter (GPF) can also produce more carbonaceous particulate matter than diesel vehicles equipped with diesel particulate filter (DPF) (Platt et al. 2017). To force adoption of technologies that

further reduce emissions, a nonvolatile particle number (PN) emission limit (UNECE Regulation 83 Suppl. 7) has been implemented. The limit is determined using the UN/ECE Particulate Measurement Programme (PMP) protocol (Andersson et al. 2007).

The PMP protocol requires a Volatile Particle Remover (VPR) as a subcomponent of a solid particle emissions measurement system, whose primary purpose is to remove hydrocarbons (HCs) in the form of semivolatile particulate matter from the sampled gas stream before measuring the solid particles. Initially only particles larger than 23 nm were subject to the protocol primarily because DPFs can efficiently remove smaller particles, and to a lesser extent, to reduce measurement variability (Andersson et al. 2007). Subsequent work has shown issues with the standard VPR methodology. For example, incomplete evaporation or evaporation followed by re-nucleation

CONTACT Adam M. Boies a.boies@eng.cam.ac.uk Department of Engineering, University of Cambridge, Trumpington Street, Cambridge, CB2 1PZ UK.

*Current affiliation: National Energy Technology Laboratory, Morgantown, West Virginia, USA

Supplemental data for this article is available online at <https://doi.org/10.1080/02786826.2021.1909700>

© 2021 The Author(s). Published with license by Taylor & Francis Group, LLC.

This is an Open Access article distributed under the terms of the Creative Commons Attribution License (<http://creativecommons.org/licenses/by/4.0/>), which permits unrestricted use, distribution, and reproduction in any medium, provided the original work is properly cited.

may occur, which results in the detection of semivolatile particles downstream of the VPR (Herner, Robertson, and Ayala 2007; Johnson et al. 2009; Giechaskiel et al. 2010; Zheng et al. 2012)

Many studies recommend the catalytic stripper (CS), originally proposed by Abdul-Khalek and Kittelson (1995) as a promising alternative to the evaporation tube in the standard VPR system. A catalytic stripper relies on evaporation and catalytic oxidation to more efficiently remove semivolatile species from the sample compared to thermal treatment alone. As such it is less prone to measurement artifacts such as semivolatile particle nucleation, heterogeneous condensation of vapor or solid particle artifacts due to charring or pyrolysis reactions within semivolatile particles (Swanson and Kittelson 2010). Further, the CS can be configured in a system that satisfies all performance requirements under PMP protocol and exhibits competitive performance in removing semivolatile particles than a evaporation tube for laboratory-generated particles (Khalek and Bougher 2011; Swanson et al. 2013) and diesel exhaust (Kittelson et al. 2005; Amanatidis et al. 2013; Ntziachristos et al. 2013). The CS can be configured in a package that is compact and lightweight. For example, Swanson et al. (2013) described the design of a miniature CS that fully removes semivolatile particles as large as 220 nm at a concentration of 10,000 part/cm³, which exceeds the PMP performance requirements of a VPR. Compact CS designs that lead to portable instruments are important in the context of the EU Real Driving Emissions (RDE) regulation in September 2017 (EU 2017) to measure vehicle emissions in real-world driving as part of the emissions type-approval process as the RDE regulations set limits on the number of solid particles emitted by light- and heavy-duty vehicles.

However, several studies recommend taking extra care when operating a CS particularly for sub-23 nm particles to mitigate conditions such as incomplete evaporation (Amanatidis et al. 2013), fuel-rich conditions (Mamakos et al. 2013), gasoline exhaust (Ntziachristos et al. 2013) and without adequate sulfur treatment (Amanatidis et al. 2018). Zheng et al. (2011) observed considerably fewer particles in the range of 3 to 10 nm downstream of CS than those after the AVL advanced particle counter. For sub-23 nm particles, the CS may increase the measurement uncertainty due to highly size-dependent tradeoff between particle losses and HC removal efficiency (Swanson and Kittelson 2010; Amanatidis et al. 2013). Depending on the mean particle size, the CS and evaporation tube can differ by around 50–150% for

the sub-23 nm emissions, which motivates better regulations such as introducing minimum permitted penetration (Giechaskiel et al. 2017). Despite several implications based on the experimental studies, particles and species behaviors in the CS are not fully understood as no detailed 2D numerical study has been conducted. Solid particle losses are size dependent as a result of strong interplay among the advection, diffusion and thermophoresis affecting the particle mobility inside the monolith channel and during cooling. To substantiate the underlying rationale behind the tradeoff between particle penetration and HC removal efficiencies, modeling particle and species transport as well as flow and thermal distributions through the device is essential.

The CS consists of two sections, within which three processes occur. The first section of the catalyst consists of a metal tube with an external heater. In this heating section, semivolatile particles and HCs absorbed to the surfaces of soot particles are evaporated and transformed into gas phase HCs. The second section of the CS is the catalytic monolith channel. In this section, the HCs diffuse to the walls, driven by a concentration gradient described by Fick's law. At the wall, HCs are oxidized by platinum group metals (PGM), which converts the HCs into CO₂ and H₂O. Alongside HCs, solid particles (particularly smaller particles) are also lost to the wall due to diffusion and thermophoresis.

This study develops a computational fluid dynamics (CFD) model of the CS, compares model results with experimental data, and optimizes the CS in terms of particle penetration and HC removal efficiencies. We employed a multiscale approach which accounts for macroscopic flow and thermal distribution and microscopic particle and species behavior inside the catalyst, separately. Velocity and temperature fields are solved independently from the macroscopic computational domain and used as a decoupled field to solve the diffusion and deposition of solid particles and HCs within the system. All test conditions are within the low Reynolds regime ($Re < 900$). The solid particle penetration and HCs removal efficiency from the CFD model were validated with the experimental results. The verified model with the experiments was employed in a parametric study to investigate the tradeoff between particle penetration and HC removal efficiency in terms of inlet flow rate and catalyst length.

2. Experimental methods

This section introduces the experimental setup for measuring solid particle penetration and hydrocarbon

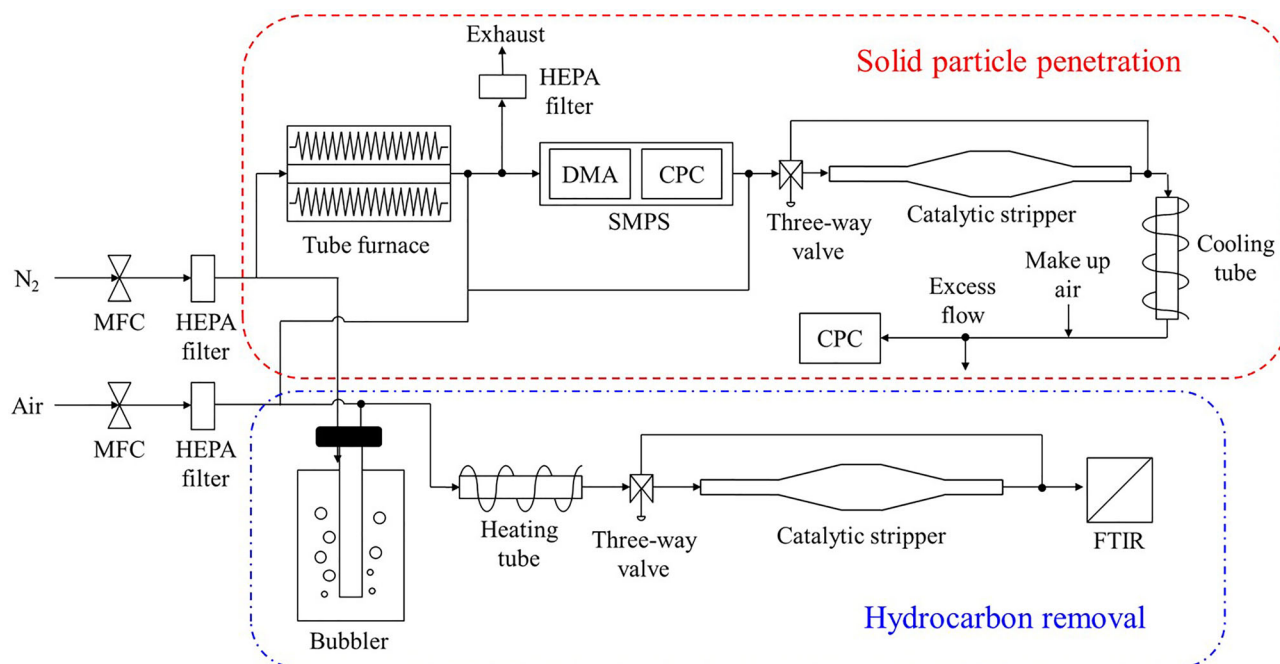


Figure 1. Schematic of measurement for solid particle penetration efficiency (upper half) and the gas phase hydrocarbon removal efficiency (lower half) of the catalytic stripper.

removal of a commercially available catalytic stripper. Catalytic Instruments GmbH & Co.KG provided a catalytic stripper encased in a heated stainless-steel tube with a conical inlet and exit region with variable monolith length. The inner diameter of inlet and outlet is 4.58 mm, and the inner diameter of the expanded region is 13 mm where the catalyst is placed at the right end. The total length of the CS is 165 mm. The reference length of catalyst l_{cat} is 19.5 mm, which will be used as a variable in the parametric study in Subsection 4.4.

2.1. Measurement of solid particle penetration

Silver nanoparticles produced in a tube furnace by an evaporation and condensation method were used to determine the solid particle penetration efficiency of the catalytic stripper. As shown in Figure 1a small amount of silver on a ceramic crucible was placed in a ceramic tube in the tube furnace. The temperature of the furnace was maintained at $T = 1100\text{--}1200^\circ\text{C}$. Nitrogen (N_2) dilution flow was varied to obtain the desired particle size and concentration in the effluent flow. Generated silver particles are size selected using a Differential Mobility Analyzer (DMA) and passed through the catalytic stripper. An ultrafine Condensation Particle Counter (CPC), model 3776 supplied by TSI connected with a three-way valve was used to measure particle concentration at the inlet and outlet of the catalytic stripper. The length of the

cooling tube between the CS outlet and CPC is 15 cm. Solid particle penetration efficiency was calculated by dividing penetrated particle concentration by inlet concentration. This experiment was conducted for hot (350°C) and cold (room temperature) conditions. The hot temperature was defined by the measured wall temperature at the location of the catalyst with an offset calibrated to allow a centerline temperature. The thermophoretic loss existing in the hot operation of CS was estimated by comparing particle penetrations in hot and cold operations.

2.2. Measurement of gas phase HCs removal

There are variations in the literature in terms of the total number of HC species measured from the engine exhaust. Some studies focus solely on the dominant species, whereas others included minor species which were orders of magnitudes lower in concentration. Overall, we have found around 105 HC species in the engine exhaust volatile organic compounds (VOCs) literature. The ten most prominent HC species in the literature are presented in Table S1 (see the online supplementary information [SI]) in descending order. Considering their relative abundance in the exhaust and saturation ratio, we selected two VOC species (Toluene, Benzene) for gas phase HC removal efficiency testing of the catalytic stripper.

As shown in Figure 1, selected HC solutions (toluene or benzene) were kept in a bubbler with

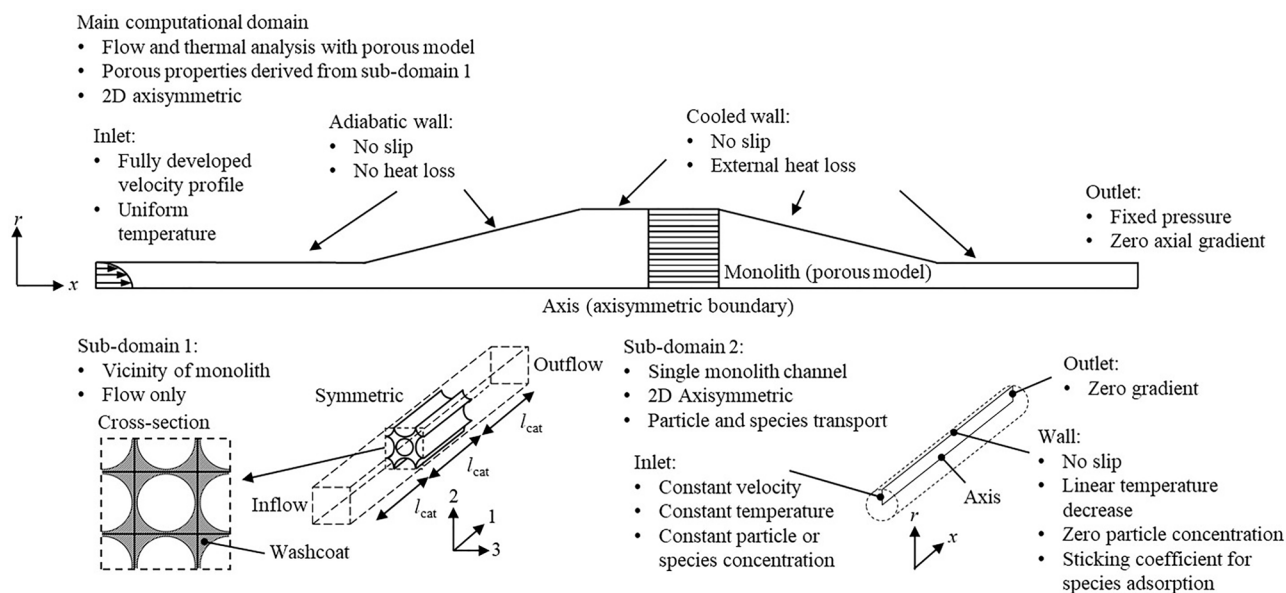


Figure 2. The schematics for the multiscale modeling of a catalytic stripper. The main computational domain for macroscopic simulations is two-dimensional axisymmetric and covers the entire structure of catalytic stripper device. The subdomain 1 is designed to estimate the porous model parameters for macroscopic model. The resulting velocity and temperature from macroscopic models are utilized in microscopic models in subdomain 2 for particle/species calculations.

controlled N_2 gas flow through the solution. Evaporated HC and N_2 gas mixtures were then diluted with compressed air. Alicat mass flow controllers (MFC) were used to precisely control N_2 and air flow rate, and therefore, the HC concentration in the stream. The HC contained air stream was fed through the catalytic stripper, and HC concentrations at the inlet and outlet were measured using a Multigas 2030 FTIR supplied by MKS. An additional heating tube was added to the inlet of the catalytic stripper for a higher flow rate (above 3 L/min) in order to maintain the gas temperature (350°C). The HC removal efficiency of the catalytic stripper was determined in accordance with $\eta_{HC} = (c_{in} - c_{out})/c_{in}$.

3. Numerical methodology

3.1. Solution strategy

The multiscale physical phenomena in the catalytic stripper device have been simulated by a combination of macroscopic and microscopic models. Figure 2 displays the schematics of computational domains and boundary conditions. The macroscopic model approximates the solid and void parts of the catalytic monolith as a porous zone wherein the porosity is the measure of the void fraction. The porous model applies realistic momentum resistance despite simplification of the complex geometry that requires large number of mesh cells to resolve the transport phenomena inside the microstructure. The momentum

resistance in the porous model is modeled by two parameters which are obtained from the microscopic simulations of flow through the porous structure depicted as subdomain 1. The macroscopic model is based on a two-dimensional axisymmetric computational domain. The boundary condition of the left side of the domain is inlet where the fully developed parabolic velocity profile and uniform temperature profile are given.

The wall temperature boundary conditions were chosen such that the axial gas temperature profile matched the experimentally measured profile. The experimental version has a coiled heater such that it is not continuous, but the high thermal conductivity of the outer casing (stainless steel) allows for a model representation of the device as having a uniform boundary. However, to obtain the experimentally measured temperature profile ending the heater at the inlet to the monolith provided the best match to thermocouple measurements from the experimental device. The wall between the inlet and the end of the conical expansion is set to adiabatic, while the wall after the conical expansion is set to cooled wall. The right side of the domain is outlet. Thus, the macroscopic model solves the overall flow and temperature distributions inside the catalytic stripper device in terms of various flow rates. The resulting velocity and temperature are fed to the microscopic models in subdomain 2 to obtain the solid particle penetration and hydrocarbon removal through the catalyst. For both

macroscopic and microscopic simulations, OpenFOAM v6 (OpenFOAM6) is chosen as a modeling platform.

The subdomain 1 for microscopic simulations covers the vicinity of the monolith channel. The length of the computational domain in flow direction (axis 1) is three times of the catalyst length l_{cat} to include the flow before and after the catalyst. The inlet and outlet boundary conditions are specified at the end of each side of domain in flow direction. The microstructure of the monolith channel is set by a representative element corresponding to a vicinity of a single monolith channel. The four surrounding sides of the representative channel are mirrored with the symmetric boundary condition. For modeling washcoat inside the channels, the open cross-sectional area of catalyst is assumed to be a circular shape whose diameter equals the inner channel width. The flow between the microstructure is solved in the subdomain 1 to estimate the porous properties for macroscopic models and is verified by the macroscopic model that applies the estimated parameters.

Species or particle transport is calculated by the microscopic model in subdomain 2 that corresponds to the inner part of the single representative channel. The inside of the circular channel is simplified by two-dimensional axisymmetric domain. The velocity and temperature at the entrance of the monolith are obtained from the macroscopic simulations. Those and the constant particle/species concentration are given as the inlet boundary condition of subdomain 2. It is assumed that semivolatile particles completely evaporate in the heating section of the CS. HC catalytic oxidation is modeled by conversion coefficient representing the fraction of HC that is oxidized which is incident to the surface of the catalyst wall. For solid particles, the boundary condition at the wall is zero concentration, while the adsorption of species is modeled by a conversion coefficient. The linearly decreasing temperature profiles based on the temperatures at each side of the catalyst predicted by macroscopic simulations are given as wall boundary conditions for temperature.

3.2. Macroscopic model

The macroscopic simulations are based on the porous model assuming the porous medium as a representative elementary volume comprised of solid and fluid parts with the porosity ε . While the porousSimpleFoam is a default solver in OpenFOAM, we employed the modifiedPorousSimpleFoam (Woo,

Kim, and Kim 2012) that solves the physical velocity \mathbf{u} instead of the superficial velocity \mathbf{U} . The physical velocity formulation allows intuitive coupling equations for modeling multi-physics simulations inside the porous media. The continuity and momentum equations of the modifiedPorousSimpleFoam are

$$\nabla \cdot (\varepsilon \rho \mathbf{u}) = 0, \quad (1)$$

$$\begin{aligned} \nabla \cdot (\varepsilon \rho \mathbf{u} \mathbf{u}) = & -\varepsilon \nabla p + \nabla \cdot (\varepsilon \mu \nabla \mathbf{u}) \\ & - \varepsilon \left(\mu c_D + \frac{1}{2} \rho |\mathbf{u} \cdot \mathbf{u}| c_F \right) \mathbf{u}. \end{aligned} \quad (2)$$

The superficial velocity \mathbf{U} defined in the porousSimpleFoam is replaced by $\varepsilon \mathbf{u}$ in the modifiedPorousSimpleFoam. The third term in the right-hand side of the momentum equation represents the momentum resistance due to the porous structure. c_D and c_F which are model parameters in the Darcy–Forchheimer equation account for the linear and nonlinear increases of resistance with increasing velocity. Anisotropic c_D and c_F , which assumes there is only unidirectional resistance in flow direction, are employed.

In the framework of the porous model, energy equations for gas and solid phases are given by

$$\nabla \cdot (\varepsilon \rho \mathbf{u} h_G) = \nabla \cdot \left(\varepsilon \frac{k_G}{c_P} \nabla h_G \right) + h_{\text{int}} a (T_S - T_G), \quad (3)$$

$$\nabla \cdot ((1 - \varepsilon) k_S \nabla T_S) + h_{\text{int}} a (T_G - T_S), \quad (4)$$

where h_G , T_G and T_S represent the gas enthalpy, gas temperature and solid temperature, respectively. a is the specific surface area. Gas phase transport properties such as μ and k_G are estimated by Sutherland's law. The solid thermal conductivity k_S , corresponding to the catalyst monolith, is approximated by a correlation from Hayes, Kolaczowski, and Thomas (1992) as a function of temperature:

$$k_S = 0.9558 - 2.09 \times 10^{-4} T_S. \quad (5)$$

Heat transfer between the gas and solid phases in the porous medium is modeled by an interfacial heat transfer coefficient defined by

$$h_{\text{int}} \frac{Nu k_G}{d_H}, \quad (6)$$

where Nu is the Nusselt number and d_H is the hydraulic diameter of the channel.

3.3. Microscopic models

The microscopic models are based on the rhoSimpleFoam that is one of the default solvers in OpenFOAM designed for compressible flow and heat transport. Microscopic simulations for flow in subdomain 1 are conducted by the default rhoSimpleFoam in isothermal condition while for the microscopic simulations in subdomain 2 a species or particle transport equation is further solved, simultaneously.

3.3.1. Estimation of porous properties

The parameters required for the porous model in macroscopic simulations are estimated by microscopic simulations of the flow passing through the catalyst depicted as subdomain 1 in Figure 2. The cell density and wall thickness of the catalyst are 600 cpsi and 4 mil (0.1016 mm), which yields the inner channel width of 0.986 mm. The porosity corresponding to the washcoated microstructure as shown in Figure 2 is $\varepsilon = 0.71$. Assuming that the flow inside the porous media is unidimensional in axis 1, the momentum resistance through the porous media with L in length is modeled by Darcy–Forchheimer equation as

$$-\frac{\Delta p}{L} = \mu c_D u_1 + \frac{1}{2} \rho c_F u_1^2. \quad (7)$$

Here, Δp is the pressure difference dictated by the momentum resistance. The parameter c_D and c_F are estimated by the Δp as a function of inlet velocity obtained from microscopic simulations of flow in subdomain 1.

3.3.2. Species transport

The removal of gas phase unburned hydrocarbons is modeled by the species transport equation given by

$$\nabla \cdot (\rho \mathbf{u} y_i) = \nabla \cdot (\rho D_{i,j} \nabla y_i), \quad (8)$$

where y_i is the mass fraction of the species i , and $D_{i,j}$ is the diffusivity of species i diffusing into species j . The diffusivity for gaseous species is estimated by the Fuller correlation (Fuller, Schettler, and Giddings 1966), e.g., the diffusivity of propane in the air (Hayes and Kolaczkowski 1998) is

$$D_{\text{Propane,air}} = 5.324 \times 10^{-5} \frac{T_G^{1.75}}{p}. \quad (9)$$

The boundary condition for the species adsorbed at the wall is defined by

$$D_{i,j} \frac{\partial y_i}{\partial x_n} \Big|_{\text{wall}} = S_i \sqrt{\frac{RT_G}{2\pi m_i}} y_i. \quad (10)$$

The species adsorption is modeled by a conversion coefficient S_i which is in the range between 0 and 1.

In this study, we simplified the surface reactions by assuming a perfect conversion of the species impinging the wall due to the sufficiently high catalyst temperature and relatively low concentration of hydrocarbon species against the catalyst loading. Thus, the species removal efficiency limited by mass transfer is modeled by the species impinging with the conversion coefficient S_i instead of accounting for complex species transport in porous media (e.g., dusty-gas model) and detailed reaction kinetics therein. The flux of oxidized species from the walls, e.g., H_2O and CO_2 , are not significant enough to affect momentum transfer.

3.3.3. Particle transport

Similarly, the solid particle penetration is modeled by the particle transport equation as

$$\nabla \cdot (\rho \mathbf{u} N_p) = \nabla \cdot (\rho D_p \nabla N_p) + K_{\text{th}} \mu \nabla \cdot \left(\frac{N_p}{T_G} \nabla T_G \right), \quad (11)$$

where N_p is the particle number concentration and D_p is the diffusivity of solid particle based on the Stokes–Einstein equation as

$$D_p = \frac{k_B T_G C_c}{3\pi \mu d_p}. \quad (12)$$

C_c is the Cunningham slip correction factor (Jennings 1988) defined by

$$C_c = 1 + Kn \left[1.252 + 0.399 \exp \left(-\frac{1.10}{Kn} \right) \right], \quad (13)$$

where Kn is the Knudsen number defined by $2\lambda/d_p$. The second term in the right-hand side of Equation (11) accounts for the thermophoresis effect with the thermophoresis coefficient K_{th} (Messerer, Niessner, and Pöschl 2003) as

$$K_{\text{th}} = 2C_c C_s \frac{k_g/k_p + C_t Kn}{(1 + 3C_m Kn)(1 + 2k_g/k_p + 2C_t Kn)} \quad (14)$$

C_s , C_t and C_m are the thermal slip, temperature jump and momentum exchange coefficient, and the values correspond to 1.147, 2.20 and 1.146, respectively (Batchelor and Shen 1985). k_g and k_p are the thermal conductivities of gas and particle. The particle size is kept constant during the microscopic simulations. Since particle agglomeration, oxidation and condensation/evaporation before the catalyst are not considered in the present study, it is assumed that there is no particle loss until the particles reach the catalyst.

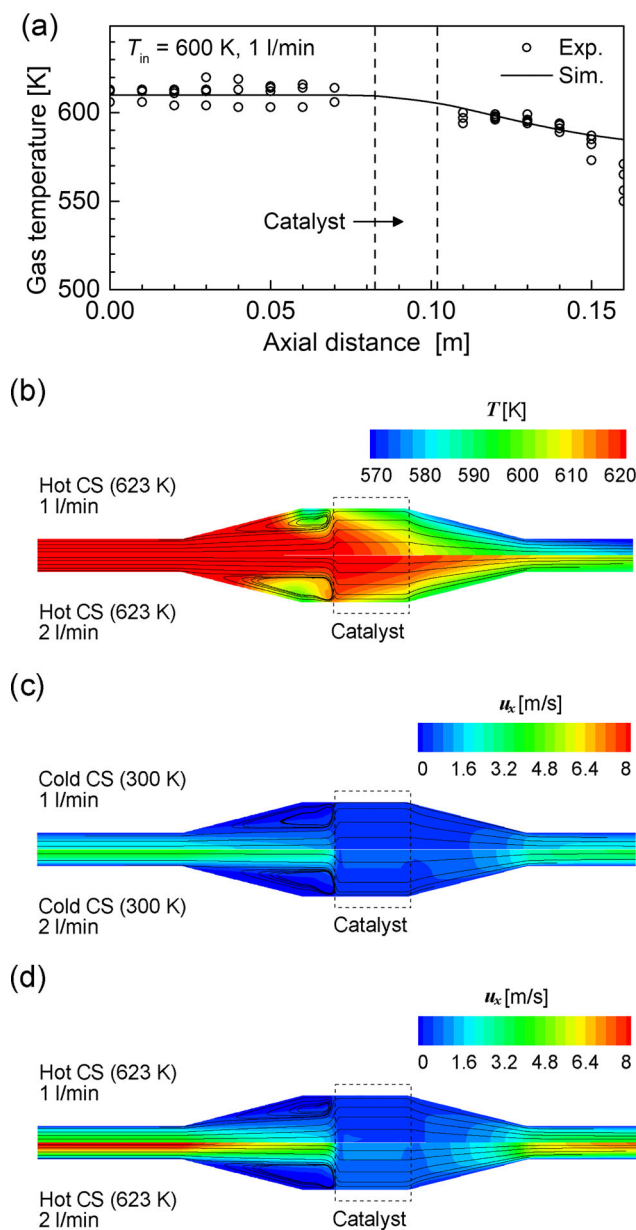


Figure 3. Results of macroscopic simulations. (a) Comparison of predicted and measured temperature profiles at the central axis. Comparisons of (b) temperature and streamline distributions for hot CS, (c) axial velocity (u_x) distributions for cold CS, and (d) u_x distributions for the hot CS with the flow rates of 1 L/min and 2 L/min.

4. Results and discussion

4.1. Flow and temperature distributions

The macroscopic simulations were performed with the porous model parameters estimated by the Darcy–Forchheimer equation (Equation (7)) and the predicted pressure drop between the catalyst in the subdomain 1. The estimation procedure of the parameters is described in SI S6 (Estimation of parameters for porous model). Figure 3 shows the results of macroscopic simulations with the estimated porous

parameter c_D . Nu is set to 3.655 that corresponds to the fully developed flow with a constant temperature boundary condition. Figure 3a compares the predicted and measured temperature profiles at the center axis of the catalytic stripper. The temperature starts decreasing at the beginning of catalyst region due to the cooled wall boundary condition defined with the external heat transfer coefficient of 1.5 and ambient temperature of 300 K. Both measured and predicted temperature profiles are in good agreement with the maximum difference of 6.8% and 4.7% for the regions before and after the catalyst.

Figures 3b–d show the results of macroscopic simulations for flow and heat transfer through the whole catalytic stripper device including the catalyst of l_{cat} (19.5 mm). In Figure 3b, the temperature near the upstream of catalyst is locally non-uniform despite no heat loss at the wall. Given the streamline, the upstream temperature distribution is dictated by the circulation of the flow before the catalyst. The results indicate that higher flow rates result in deeper heat penetration through the catalyst but also simultaneously leads to larger upstream circulation which diminishes the heat transfer into the catalyst. Figures 3c and d compare the results for two different inlet flow rates in hot (623 K) and cold (300 K) operating conditions. Note that the flow rate in the experiments is regulated before heating so that the actual velocity at the inlet depends on the operating temperature. With increasing flow rate or operating temperature, the velocity magnitude becomes higher accordingly, but the trends of velocity distributions in the four cases are similar.

Figure 4a exhibits the velocity at the entry of the catalyst and the average temperature of the catalyst with regards to the flow rate. The maximum and minimum temperatures in the error bars correspond to the temperature at the beginning and at the end of the catalyst, respectively. The entry velocity increases almost linearly with increase of flow rate as well as the operating temperature. However, as flow rate increases the average temperature for the hot operating condition increases nonlinearly and the temperature variance in the catalyst decreases as represented by the length of the error bars for hot CS. This indicates that higher flow rate results in more heat transfer to the catalyst, but the gradient in temperature decreases, which might be attributed to the increase of circulation of the velocity as shown in Figure 3b. Figure 4b shows the gas mean residence time obtained by the catalyst length divided by the catalyst entry velocity shown in Figure 4a, which results in the inverted

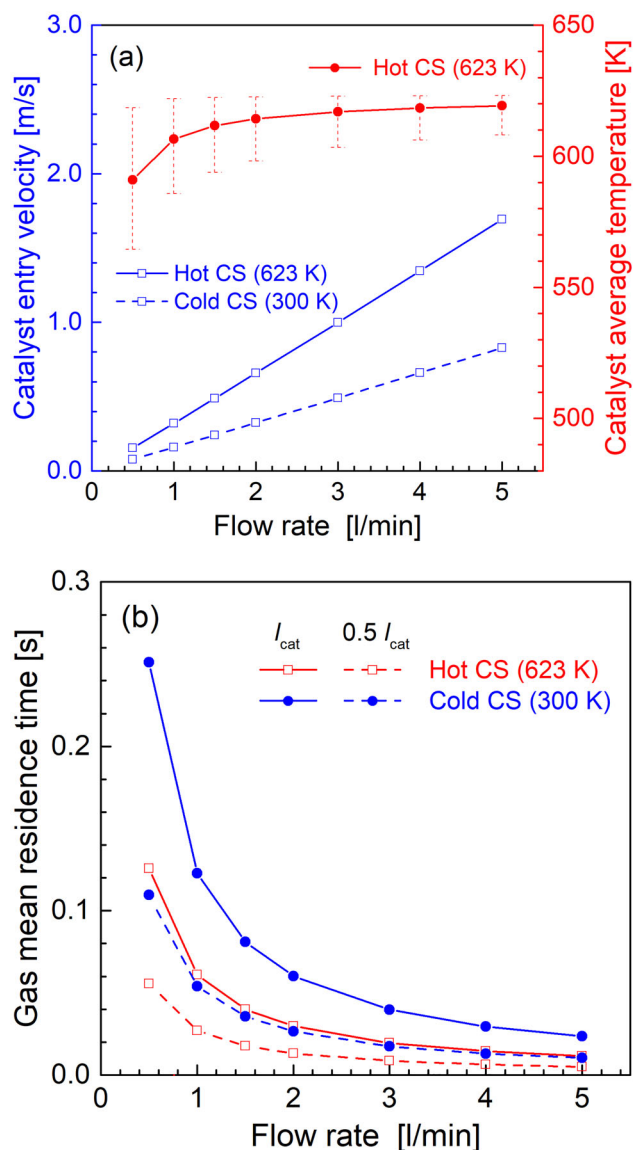


Figure 4. (a) Velocity at the entrance of catalyst for hot (623 K) and cold (300 K) operating conditions and average temperature of the catalyst for hot operating condition with regards to the flow rate. Upper and lower error bars in the temperature profile correspond to the temperature at the upstream and downstream sides of the catalyst, respectively. (b) Gas mean residence time with regards to the flow rate. Comparison of hot and cold operation and catalyst length of l_{cat} and $0.5 l_{cat}$.

trends against the velocity profile in terms of the flow rates. The residence time for hot CS with l_{cat} is similar to that for the cold CS with $0.5 l_{cat}$, which is attributed to the counterbalance of the increase of temperature and the decrease of catalyst length for those cases. The velocity and temperature in Figure 4 are used as boundary conditions for microscopic simulations of species and particles in subdomain 2.

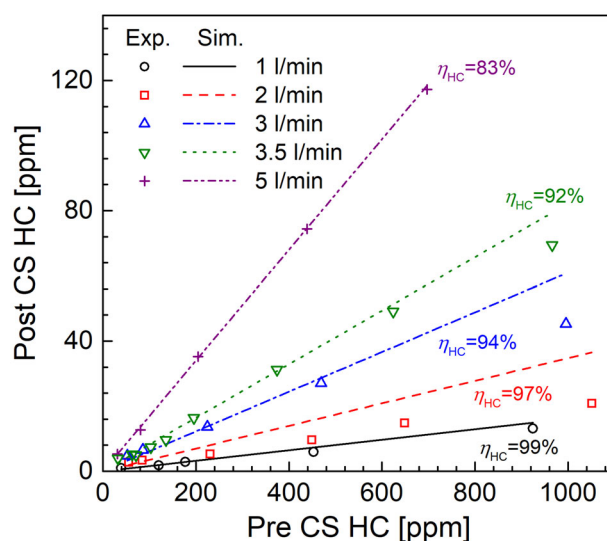


Figure 5. Measured (Exp.) and predicted (Sim.) toluene concentrations before (Pre CS) and after (Post CS) the catalytic stripper device with various flow rates. η_{HC} is predicted HC removal efficiencies for different inlet flow rate.

4.2. Hydrocarbon removal

The HC removal efficiency through the catalyst is computed by solving the species transport equations (Equation (8)) together with momentum and energy equations in the subdomain 2. Figure 5 shows the measured and predicted toluene concentrations before and after the catalytic stripper device with various flow rates. The concentration profiles in Figure 5 show almost linear relationship, which represent a hydrocarbon removal efficiency that varies from approximately 80% (5 L/min) to >99% (1 L/min) and is largely independent of inlet concentration. The dependency of inlet concentration is usually modeled by an inhibition term in the reaction rate equation to account for the retardment of the species adsorption depending on the site occupancy of the catalyst surface. By assuming no inhibition, the predicted removal efficiency in this study depends only on the flow rate. To that end, a variable conversion coefficient depending on the flow rate applies, see SI S1 (Species adsorption model with a variable conversion coefficient) for details. The maximum difference between the predicted and measured (mean) conversion efficiencies is 0.56% (see SI Figure S1). When the variable conversion coefficient model is implemented, the model generally over-predicts post-CS hydrocarbons by 2.2% (5 L/min) to 50.9% (2 L/min), thus, serving as a conservative prediction of HC removal efficiency.

The removal efficiencies for other HCs are estimated by the same model used for toluene with the selected flow rate of 1 L/min. Given that the diffusivity

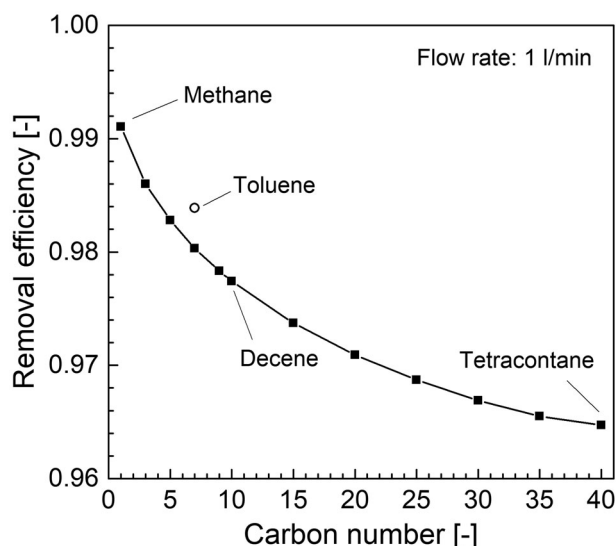


Figure 6. Predicted hydrocarbons removal efficiency with various carbon numbers (square symbols: alkanes hydrocarbon, circle: toluene). Predictions with flow rate of 1 L/min.

of the normal alkanes decreases by a factor of seven from methane to tetracontane (Johnson and Kittelson 1996), the diffusivities of alkanes HCs are estimated with the methane diffusivity at 293 K (Engineering_ToolBox 2018). Here, the diffusivity of HCs corresponds to the binary diffusion coefficient of HCs diffusing through air. Figure 6 shows the predicted HCs removal efficiency with regards to the carbon number. Increasing carbon number causing the decrease of diffusivity results in the decrease of removal efficiency. The resulting efficiency loss by increasing carbon number from 1 to 40 is 2.6%.

4.3. Solid particle penetration

The penetration of solid particles is computed by microscopic simulations solving momentum, energy and particle transport equation (Equation (11)) in the subdomain 2. Again, the boundary condition of particle at the wall is zero concentration by assuming perfect deposition of particles arrived at the wall, as usual for many analytical and numerical studies. The influence of inlet particle profiles on the diffusion loss through the single channel is investigated, see SI S2 (Particle diffusion loss through the catalyst). Among the different inlet particle profiles, a half parabolic profile led to the best agreement with the measured penetration by the average difference of 2.96%. Thus, the half-parabolic particle profile is chosen for the calculations in this section. The boundary conditions for velocity and temperature are identical to the calculations for HC removal in Subsection 4.2.

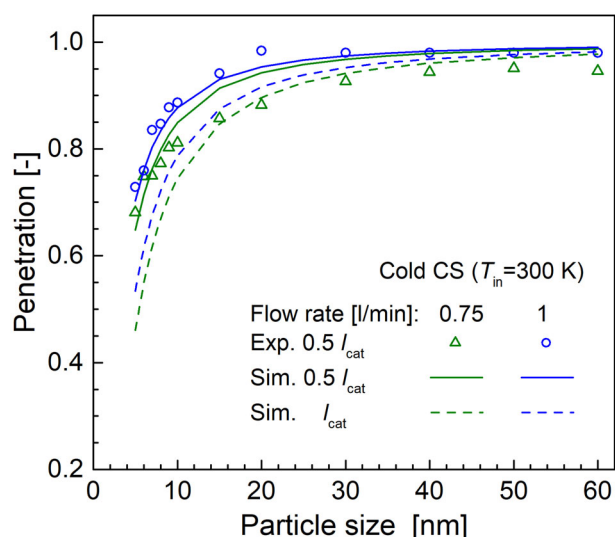


Figure 7. Predicted (Sim.) and measured (Exp.) solid particle penetration for cold operation ($T_{in} = 300$ K) of catalytic stripper with a half of the reference catalyst length ($0.5 l_{cat} = 9.75$ mm). Predictions with a reference length of the catalyst ($l_{cat} = 19.5$ mm) are compared.

Figure 7 exhibits the measured and predicted solid particle penetration for the cold operating condition (300 K) with respect to the particle size and inlet flow rate. The length of the catalyst for the results are a half of the reference length ($0.5 l_{cat} = 9.75$ mm). The range of particle size for the simulations is 5–60 nm according to the measured range of particle size. In the model, particle penetration is mainly governed by the interplay between advection and diffusion in the absence of thermophoresis. With increasing particle size, the decreasing particle diffusivity results in the increase of penetration. The penetration also increases with increasing flow rate due to the increase of advective flux in the flow direction. The predicted solid particle penetration efficiencies are generally in good agreement with the measured counterparts by average difference of 4.3% and 1.6% for the flow rate of 0.75 and 1 L/min. The penetration at the flow rate of 0.75 L/min is slightly overpredicted for the particles with $d_p > 10$ nm. Simulations with the reference catalyst length ($l_{cat} = 19.5$ mm) are also conducted for the cold operation – the penetration becomes slightly lower due to the extended path for the diffusion loss.

Before the calculations of particle penetration for hot operation, the implementation of thermophoresis model is validated with the analytic solution of particle deposition in laminar channel flow (Walker, Homsy, and Geyling 1979), see SI S3 (Validation of thermophoresis model). The thermophoretic loss is not significant inside the catalytic stripper as the temperature difference shown in Figure 3 is less than

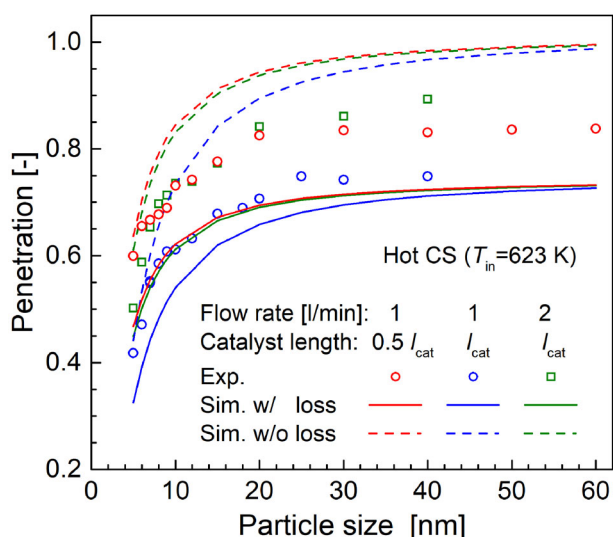


Figure 8. Predicted (Sim.) and measured (Exp.) solid particle penetration for hot operation ($T_{in} = 623$ K) of catalytic stripper with respect to particle diameter, flow rate and catalyst length ($0.5 l_{cat} = 9.75$ mm and $l_{cat} = 19.5$ mm). Simulation data with particle loss through the cooling tube after the catalytic stripper (w/loss) and without the loss (w/o loss) are compared.

50 K. However, this can be significant in the cooling tube between the catalytic stripper and the measurement device that requires room temperature. Accounting for the additional particle loss is needed to compare measured and predicted penetration. The model showed that thermophoretic loss depends on the initial particle profile as shown in Figure S4-1 and S4-2 in the SI.

Figure 8 exhibits the predicted and measured solid particle penetration in the hot operating condition (623 K). The trends of penetration in terms of particle size are similar to those of cold operation, but the values are lower due to the higher catalyst entry velocity according to the higher operating temperature. Simulation results “without loss” correspond to the predicted penetration after the catalyst, whereas “with loss” correspond to lower penetration due to the thermophoretic particle loss in the cooling tube. The cooling tube loss results in a reduction of penetration by 26.4% which is obtained with a constant particle profile at the beginning of cooling tube, while there is almost no particle loss with the parabolic particle profile. Thus, the predicted curves with and without loss indicate the range of particle penetration depending on the particle profile. The measured penetration is in between the predicted efficiency with and without loss, and the real particle profile after the catalyst might be neither constant nor fully developed. Further in-situ experimental

work is needed to determine particle concentration profiles after the monolith section. Note that, the penetrations with l_{cat} and 2 L/min (green colored) are almost equivalent to those with $0.5 l_{cat}$ and 1 L/min (red colored), which corresponds well to the similar gas residence time for the two cases, 29.7 ms and 27 ms, respectively. This trend was observed in both the measured and predicted results.

4.4. Parametric study

The computational models verified with the measured solid particle penetration and HC removal are employed in the parametric study for wider range of test conditions in terms of flow rate and catalyst length. Three representative particle sizes of 4, 10 and 23 nm are chosen instead of the particle sizes used in the experiment (5–60 nm). Particle diameters of 23 nm correspond to the current regulation with the PMP protocol. Particle diameters of 10 nm is also an important factor as many studies (Zheng et al. 2012; Giechaskiel, Lähde, and Drossinos 2019; Giechaskiel et al. 2019) report that it would be feasible to reduce the legislative threshold particle size limit to 10 nm. Giechaskiel et al. (2017) recommend guaranteeing >50% penetration of 10 nm particles to this end. Particle diameters of 4 nm corresponds to one of the limits for measuring sub-10 nm particles (CPC 3752) that shows a similar measuring pattern as for the other CPC with >50% at 10 nm particles (Giechaskiel 2019). For HC removal, methane (CH_4) and tetracontane ($C_{40}H_{82}$) are represented as the lightest and heaviest species available in the present study. The range of inlet flow rate in the parametric study is 0.5 to 5 L/min. Based on the reference catalyst length l_{cat} of 19.5 mm, the catalyst length varies by a quarter size ($0.25 l_{cat} = 4.875$ mm), a half size ($0.5 l_{cat} = 9.75$ mm) and a maximum size (29 mm) available in the current design of catalytic stripper. While all experiments confirmed that >99% of 30 nm semivolatile (tetracontane) particles are effectively removed as measured by CPCs as outlined by PMP protocol, this work measures to total gas concentration of HCs rather than those that exist solely in the particle phase. Measured semivolatile particle removal efficiency is presented in SI S7.

Figure 9 shows the penetration for the solid particles of the three representative sizes and the removal efficiencies for the two HC species with various inlet flow rate and catalyst length. The figures clearly show the tradeoff relation between solid particle penetration and HC removal in terms of changing the two

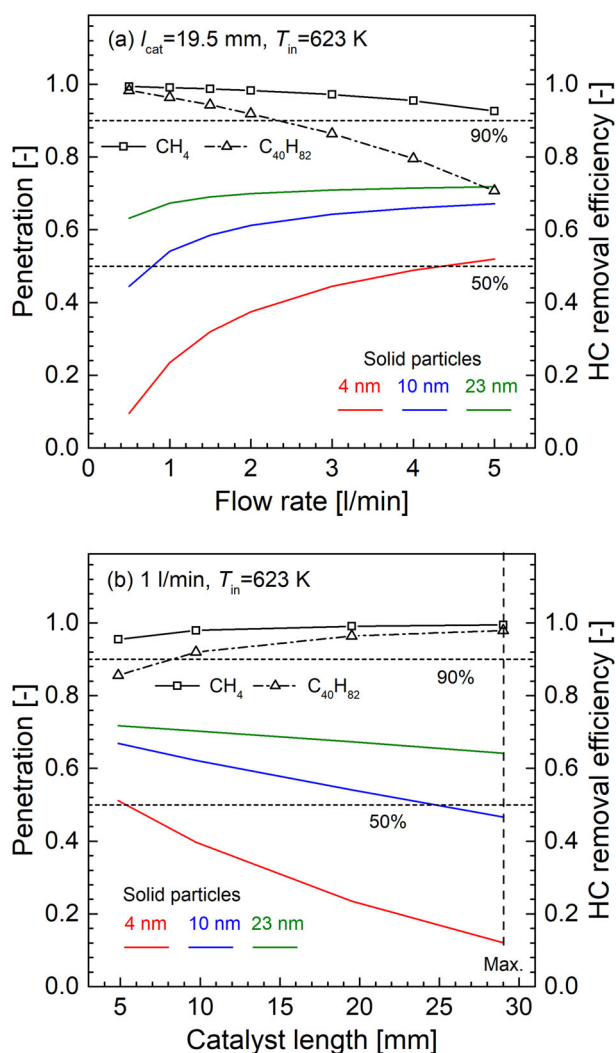


Figure 9. Results of parametric study of particle penetration and HC removal efficiency in terms of flow rate (a) and catalyst length (b). Comparison of penetration of 4 nm, 10 nm, 23 nm solid particles and removal efficiency of methane (CH_4) and tetracontane ($C_{40}H_{82}$).

parameters. In Figure 9a, the penetration of 23 nm particles is always higher than 50% for all test conditions. The penetration of 10 nm particles is mostly higher than 50% except for the inlet flow rate of 0.5 L/min. However, the >50% penetration of 4 nm particles is only achieved when the inlet flow rate is 5 L/min, which sacrifices approximately 25% of tetracontane ($C_{40}H_{82}$) removal as compared to 1 L/min of inlet flow rate. The low removal efficiency of tetracontane as compared to methane (CH_4) is due to its diffusivity, which is 7 times lower than that of methane. This causes <90% of removal efficiency when the inlet flow rate is higher than 3 L/min.

In Figure 9b, the increase of catalyst length leads to the decrease of penetration and the increase of

HC removal on the contrary to the trend of increasing inlet flow rate. The parametric study in terms of catalyst length indicates that a half size ($0.5l_{cat} = 9.75$ mm) of catalyst can effectively keep >90% of HC removal and >50% penetration of 10 nm particles in the wide range of test conditions. With $0.5l_{cat}$, the penetration improves by 16%, 8% and 3% for 4 nm, 10 nm and 23 nm particles with sacrificing 1.2% and 4.4% of methane and tetracontane removal efficiency. Note that, the increase in penetration with $0.5l_{cat}$ can be almost recovered by doubled flow rate with l_{cat} as already shown in Figure 8. The maximum difference between l_{cat} with 2 L/min and $0.5l_{cat}$ with 1 L/min is 2.2% for penetration and 0.5% for HC removal efficiency. A quarter size ($0.25l_{cat}$) and the maximum length of catalyst (29 mm) are not suitable as the quarter size ($0.25l_{cat}$) is not sufficient for HC removal, and the maximum length of catalyst (29 mm) is unable to achieve 50% penetration of 10 nm particles.

Figure 10 shows the performance maps in terms of the two test parameters that result in >50% of solid particle penetration and >90% of HC removal. The red (black), orange (dark-gray) and yellow (light-gray) regions correspond to the results of 4 nm, 10 nm and 23 nm particles, respectively. Each node point represents each test case with the two corresponding test parameters. The penetration of 23 nm particles is always higher than 50% in the whole test conditions in this study. For 10 nm, Figure 10a shows a wide range of test conditions for >50% particle penetration and >90% of methane removal. The five outliers at the bottom-right side correspond to where the methane removal is less than 90% due to the combination of short catalyst length and high flow rate. The three outliers at the top-left region correspond to <50% particle penetration due to the long catalyst. Figure 10b shows a narrower region with more outliers at the right side due to the lower diffusivity of tetracontane than methane. For 4 nm particles, Figure 10a shows only a few conditions that meet >50% of penetration and >90% of methane removal, while it is not achieved with tetracontane as shown in Figure 10b. Although this map is only valid for the catalytic strip in the present study, it clearly shows the tradeoff between particle penetration and HC removal efficiencies with various flow rate and catalyst length, which provides guidance to choose operating conditions targeting a certain amount of particle penetration and HC removal in the practical tests.

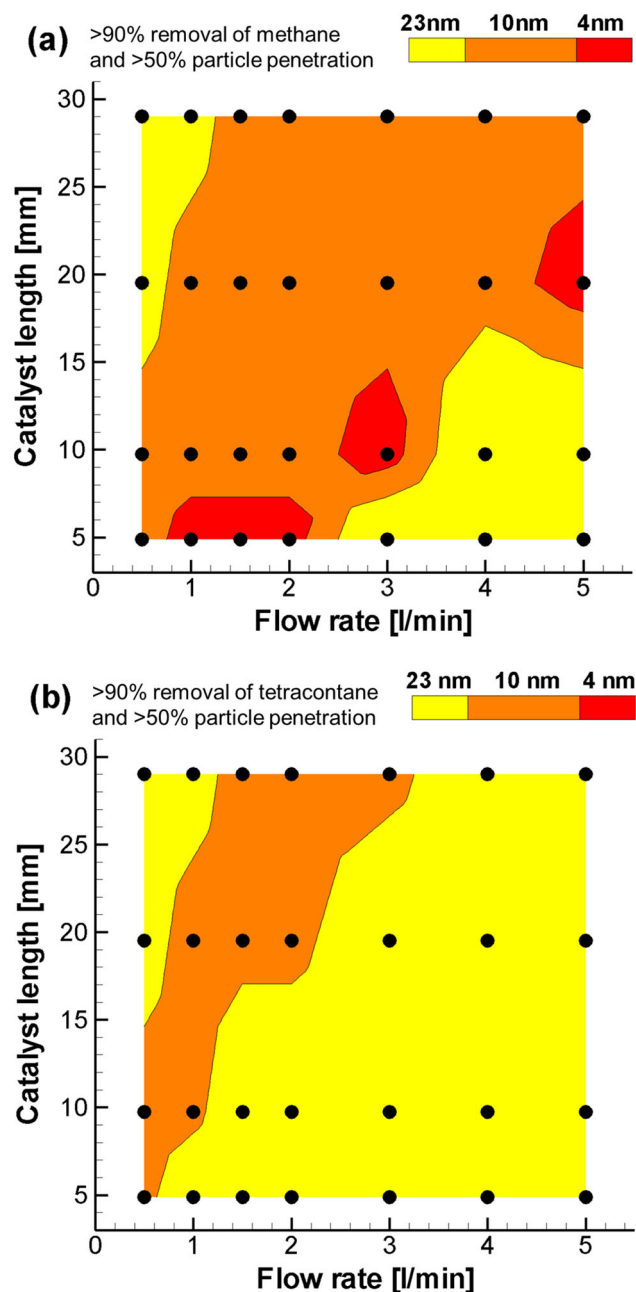


Figure 10. Performance map for >50% penetration of 4 nm, 10 nm and 23 nm particles and >90% removal efficiency for methane (a) and tetracontane (b) in terms of inlet flow rate and catalyst length.

5. Conclusions

This study aimed to develop a computational model for a catalytic stripper with a view to understanding the relation between solid particle penetration and HCs removal under various operating conditions. We employed a multiscale modeling approach that consists of macroscopic for overall behaviors of flow and temperature through the catalytic stripper and

microscopic models for the particle penetration and hydrocarbon removal performance.

The macroscopic simulations provide a clear insight into the velocity and temperature distribution through the device with the external heat loss fitted to match the measured axial temperature profile. A circulating flow pattern is observed before the catalyst due to the momentum resistance of the catalyst. Higher flow rate leads to deeper heat penetration through the catalyst but also causes a larger circulating flow before the catalyst which obstructs heat penetration, simultaneously. Consequently, the average temperature of the catalyst nonlinearly increases with increasing flow rate.

For modeling the HC removal efficiency, a variable conversion coefficient in terms of velocity is introduced without consideration of catalytic reactions. With the best fit conversion coefficient, the predicted post-CS hydrocarbons are slightly overestimated by 2.2% to 50.9% depending on the inlet flow rate. The solid particle penetration in the cold operation (300 K) is mainly governed by the interplay between the advection and diffusion inside the catalyst. It is noted that the penetration strongly depends on the particle profile – parabolic particle profile results in higher penetration than constant profile. In the hot operation (623 K), thermophoresis is not significant inside the catalyst but significant in the cooling tube between the catalytic stripper and the measurement device where the hot stream cools down to the room temperature. The additional thermophoretic loss is up to 26.4% that correspond to the constant particle profile after the catalyst. Measured penetration is in the range between the predicted penetration through the catalyst and the penetration when corrected for thermophoretic loss. A comprehensive model that combines both microscopic and macroscopic models for particle transport requires future development to numerically analyze the local particle distribution dictated by thermophoresis through the entire device.

With the established models, a parametric study of inlet flow rate and catalyst length was conducted with a view to providing a clear insight into the tradeoff relation in particle penetration and HC removal efficiencies. The performance of the reference length (19.5 mm) of the catalyst with 2 L/min of flow rate is almost equivalent to that of a half-length (9.75 mm) of catalyst with 1 L/min. This was also observed from the experiments. The results indicate that >50% penetration of 23 nm particles with >90% HC removal is achievable in all of the test conditions in this study. Such performance is feasible for 10 nm particles in a

wide range of test conditions, but for only very limited conditions for 4 nm particles. Although the numerical model is unable to account for the removal of semivolatile particles by assuming complete evaporation of those particles before the catalyst, the experiments confirmed that >99% removal of 30 nm semivolatile (tetracontane) particles is achieved, which satisfies the regulatory limit of PMP protocol. The findings in the present study can provide fundamental guidance to the proper operating conditions for both particle penetration and HC removal in the practical usage of catalytic stripper.

Nomenclature

a	specific surface area, m^{-1}
C_C	Cunningham slip correction factor, –
c	concentration, mol m^{-3}
c_D	Darcy coefficient in Darcy–Forchheimer equation, m^{-2}
c_F	Forchheimer coefficient in Darcy–Forchheimer equation, m^{-1}
c_p	heat capacity, $\text{J kg}^{-1} \text{K}^{-1}$
d_H	hydraulic diameter, m
$D_{i,j}$	diffusivity of species i diffusing into species j , $\text{m}^2 \text{s}^{-1}$
D_P	particle diffusivity, $\text{m}^2 \text{s}^{-1}$
d_P	particle diameter, m
h	enthalpy, N m
h_{int}	interface heat transfer coefficient, $\text{W m}^{-2} \text{K}^{-1}$
K_{th}	thermophoresis coefficient, –
k	thermal conductivity, $\text{W m}^{-1} \text{K}^{-1}$
k_B	Boltzmann constant, J K^{-1}
L	length of catalyst, m
m	molecular weight, g mol^{-1}
N_P	particle number concentration, m^{-3}
p	pressure, N m^{-2}
R	universal gas constant, $\text{J mol}^{-1} \text{K}^{-1}$
S_i	conversion coefficient of species i , –
T	temperature, K
\mathbf{u}	velocity field $\mathbf{u} = (u_1, u_2, u_3)\text{T}$, m s^{-1}
x	Cartesian coordinate, m
y_i	mass fraction of species i , –

Greek symbols

ε	porosity, –
η_{HC}	hydrocarbon removal efficiency, –
μ	viscosity, $\text{kg m}^{-1} \text{s}^{-1}$
ρ	density, kg m^{-3}

Subscripts

G	gas phase
in	inlet
i, j	species indices
n	normal
p	particle
S	solid phase
w	wall

Acknowledgment

Catalytic Instruments GmbH & Co.KG provided the catalytic strippers used and technical guidance associated with changing lengths.

Funding

This work was supported by Portable Nano-Particle Emission Measurement System (PEMs4Nano) project from European Union's Horizon 2020 research and innovation programme (Grant Agreement no. 724145) and Innovate UK (project ref: 103304). Additional support was provided by the Engineering and Physical Sciences Research Council Centre for Sustainable Road Freight (EP/R035199/1).

ORCID

Mino Woo  <http://orcid.org/0000-0002-6799-6223>
 Jacob Swanson  <http://orcid.org/0000-0002-5086-1373>
 Marc E. J. Stettler  <http://orcid.org/0000-0002-2066-9380>
 Adam M. Boies  <http://orcid.org/0000-0003-2915-3273>

References

- Abdul-Khalek, I. S., and D. B. Kittelson. 1995. *Real time measurement of volatile and solid exhaust particles using a catalytic stripper*. SAE International. SAE Technical Paper 950236. doi: [10.4271/950236](https://doi.org/10.4271/950236).
- Amanatidis, S., L. Ntziachristos, B. Giechaskiel, D. Katsaounis, Z. Samaras, and A. Bergmann. 2013. Evaluation of an oxidation catalyst (“catalytic stripper”) in eliminating volatile material from combustion aerosol. *J. Aerosol Sci.* 57:144–55. doi: [10.1016/j.jaerosci.2012.12.001](https://doi.org/10.1016/j.jaerosci.2012.12.001).
- Amanatidis, S., L. Ntziachristos, P. Karjalainen, E. Saukko, P. Simonen, N. Kuittinen, P. Aakko-Saksa, H. Timonen, T. Rönkkö, and J. Keskinen. 2018. Comparative performance of a thermal denuder and a catalytic stripper in sampling laboratory and marine exhaust aerosols. *Aerosol Sci. Technol.* 52 (4):420–32. doi: [10.1080/02786826.2017.1422236](https://doi.org/10.1080/02786826.2017.1422236).
- Andersson, J., B. Giechaskiel, R. Munoz Bueno, E. Sandbach, and P. Dilara. 2007. Particle Measurement Programme (PMP) Light-duty Inter-laboratory Correlation Exercise (ILCE_LD) Final Report. EUR 22775 EN. 2007. JRC37386.
- Batchelor, G. K., and C. Shen. 1985. Thermophoretic deposition of particles in gas flowing over cold surfaces. *J. Colloid Interface Sci.* 107 (1):21–37. doi: [10.1016/0021-9797\(85\)90145-6](https://doi.org/10.1016/0021-9797(85)90145-6).
- Engineering_ToolBox. 2018. Diffusion coefficients of gases in excess of air.
- EU. 2017. Commission regulation (eu) 2017/1151 of 1 June 2017 supplementing Regulation (EC) No 715/2007 of the European Parliament and of the Council on type-approval of motor vehicles with respect to emissions from light passenger and commercial vehicles (Euro 5 and Euro 6) and on access to vehicle repair and maintenance information, amending Directive 2007/46/EC of the

- European Parliament and of the Council, Commission Regulation (EC) No 692/2008 and Commission Regulation (EU) No 1230/2012 and repealing Commission Regulation (EC) No 692/2008 (Text with EEA relevance).
- Fuller, E. N., P. D. Schettler, and J. C. Giddings. 1966. New method for prediction of binary gas-phase diffusion coefficients. *Ind. Eng. Chem.* 58 (5):18–27. doi: 10.1021/ie50677a007.
- Giechaskiel, B. 2019. Differences between tailpipe and dilution tunnel sub-23 nm nonvolatile (solid) particle number measurements. *Aerosol Sci. Technol.* 53 (9):1012–22. doi: 10.1080/02786826.2019.1623378.
- Giechaskiel, B., R. Chirico, P. F. DeCarlo, M. Clairrotte, T. Adam, G. Martini, M. F. Heringa, R. Richter, A. S. H. Prevot, U. Baltensperger, et al. 2010. Evaluation of the particle measurement programme (pmp) protocol to remove the vehicles' exhaust aerosol volatile phase. *Sci. Total Environ.* 408 (21):5106–16. doi: 10.1016/j.scitotenv.2010.07.010.
- Giechaskiel, B., T. Lähde, and Y. Drossinos. 2019. Regulating particle number measurements from the tailpipe of light-duty vehicles: The next step? *Environ. Res.* 172:1–9. doi: 10.1016/j.envres.2019.02.006.
- Giechaskiel, B., A. Mamakos, J. Woodburn, A. Szczotka, and P. Bielaczyc. 2019. Evaluation of a 10 nm particle number portable emissions measurement system (PEMS). *Sensors (Basel)* 19 (24):5531. doi: 10.3390/s19245531.
- Giechaskiel, B., J. Vanhanen, M. Väkevää, and G. Martini. 2017. Investigation of vehicle exhaust sub-23 nm particle emissions. *Aerosol Sci. Technol.* 51 (5):626–41. doi: 10.1080/02786826.2017.1286291.
- Hayes, R. E., and S. T. Kolaczowski. 1998. *Introduction to catalytic combustion*. Gordon and Breach Science Publishers. ISBN: 90-5699-092-6.
- Hayes, R. E., S. T. Kolaczowski, and W. J. Thomas. 1992. Finite-element model for a catalytic monolith reactor. *Comput. Chem. Eng.* 16 (7):645–57. doi: 10.1016/0098-1354(92)80014-Z.
- Herner, J. D., W. H. Robertson, and A. Ayala. 2007. Investigation of ultrafine particle number measurements from a clean diesel truck using the European PMP protocol. SAE International. SAE Technical Paper 2007-01-1114.
- Jennings, S. G. 1988. The mean free path in air. *J. Aerosol Sci.* 19 (2):159–66. doi: 10.1016/0021-8502(88)90219-4.
- Johnson, J. E., and D. B. Kittelson. 1996. Deposition, diffusion and adsorption in the diesel oxidation catalyst. *Appl. Catal. B* 10 (1–3):117–37. doi: 10.1016/0926-3373(96)00027-6.
- Johnson, K. C., T. D. Durbin, H. Jung, A. Chaudhary, D. R. Cocker, J. D. Herner, W. H. Robertson, T. Huai, A. Ayala, and D. Kittelson. 2009. Evaluation of the European PMP methodologies during on-road and chassis dynamometer testing for DPF equipped heavy-duty diesel vehicles. *Aerosol Sci. Technol.* 43 (10):962–9. doi: 10.1080/02786820903074810.
- Khalek, I. A., and T. Bougher. 2011. Development of a solid exhaust particle number measurement system using a catalytic stripper technology. *SAE Int. J. Engines* 4 (1): 610–8. doi: 10.4271/2011-01-0635.
- Kittelson, D. B., W. F. Watts, J. C. Savstrom, and J. P. Johnson. 2005. Influence of a catalytic stripper on the response of real time aerosol instruments to diesel exhaust aerosol. *J. Aerosol Sci.* 36 (9):1089–107. doi: 10.1016/j.jaerosci.2004.11.021.
- Künzi, L., M. Krapf, N. Daher, J. Dommen, N. Jeannet, S. Schneider, S. Platt, J. G. Slowik, N. Baumlin, M. Salathe, et al. 2015. Toxicity of aged gasoline exhaust particles to normal and diseased airway epithelia. *Scientific Reports.* 5:11801. doi: 10.1038/srep11801.
- Mamakos, A., I. Khalek, R. Giannelli, and M. Spears. 2013. Characterization of combustion aerosol produced by a mini-cast and treated in a catalytic stripper. *Aerosol Sci. Technol.* 47 (8):927–36. doi: 10.1080/02786826.2013.802762.
- Messerer, A., R. Niessner, and U. Pöschl. 2003. Thermophoretic deposition of soot aerosol particles under experimental conditions relevant for modern diesel engine exhaust gas systems. *J. Aerosol Sci.* 34 (8):1009–21. doi: 10.1016/S0021-8502(03)00081-8.
- Ntziachristos, L., S. Amanatidis, Z. Samaras, B. Giechaskiel, and A. Bergmann. 2013. Use of a catalytic stripper as an alternative to the original PMP measurement protocol. *SAE Int. J. Fuels Lubr.* 6 (2):532–41. doi: 10.4271/2013-01-1563.
- OpenFOAM6. OpenFOAM v6. 2018. The OpenFOAM Foundation Ltd. Available from: <https://openfoam.org/version/6/>.
- Platt, S. M., I. E. Haddad, S. M. Pieber, A. A. Zardini, R. Suarez-Bertoa, M. Clairrotte, K. R. Daellenbach, R. J. Huang, J. G. Slowik, S. Hellebust, et al. 2017. Gasoline cars produce more carbonaceous particulate matter than modern filter-equipped diesel cars. *Sci. Rep.* 7 (1):4926. doi: 10.1038/s41598-017-03714-9.
- Swanson, J., and D. Kittelson. 2010. Evaluation of thermal denuder and catalytic stripper methods for solid particle measurements. *J. Aerosol Sci.* 41 (12):1113–22. doi: 10.1016/j.jaerosci.2010.09.003.
- Swanson, J., D. Kittelson, B. Giechaskiel, A. Bergmann, and M. Twigg. 2013. A miniature catalytic stripper for particles less than 23 nanometers. *SAE Int. J. Fuels Lubr.* 6 (2):542–51. doi: 10.4271/2013-01-1570.
- Walker, K. L., G. M. Homsy, and F. T. Geyling. 1979. Thermophoretic deposition of small particles in laminar tube flow. *J. Colloid Interface Sci.* 69 (1):138–47. doi: 10.1016/0021-9797(79)90088-2.
- Woo, M., C. Kim, and G. Kim. 2012. Consideration on heat and reaction in metal foam. In *7th OpenFOAM workshop*. Germany: Technische Universität Darmstadt.
- Zheng, Z., T. D. Durbin, G. Karavalakis, K. C. Johnson, A. Chaudhary, D. R. Cocker, J. D. Herner, W. H. Robertson, T. Huai, A. Ayala, et al. 2012. Nature of sub-23-nm particles downstream of the European particle measurement programme (pmp)-compliant system: A real-time data perspective. *Aerosol Sci. Technol.* 46 (8):886–96. doi: 10.1080/02786826.2012.679167.
- Zheng, Z., K. C. Johnson, Z. Liu, T. D. Durbin, S. Hu, T. Huai, D. B. Kittelson, and H. S. Jung. 2011. Investigation of solid particle number measurement: Existence and nature of sub-23nm particles under PMP methodology. *J. Aerosol Sci.* 42 (12):883–97. doi: 10.1016/j.jaerosci.2011.08.003.